Relationship between Hard and Soft X-ray Emission Components of a Solar Flare

Jingnan Guo [1,2,3], Siming Liu [1,3], Lyndsay Fletcher [1], and Eduard P. Kontar [1]

ABSTRACT

X-ray observations of solar flares routinely reveal an impulsive high-energy and a gradual low-energy emission component, whose relationship is one of the key issues of solar flare study. The gradual and impulsive emission components are believed to be associated with, respectively, the thermal and nonthermal components identified in spectral fitting. In this paper, a prominent ~ 50 second hard X-ray (HXR) pulse of a simple GOES class C7.5 flare on 20 February 2002 is used to study the association between high energy, non-thermal and impulsive evolution, and low energy, thermal and gradual evolution. We use regularized methods to obtain time derivatives of photon fluxes to quantify the time evolution as a function of photon energy, obtaining a break energy between impulsive and gradual behavior. These break energies are consistent with a constant value of ~ 11 keV in agreement with those found spectroscopically between thermal and non-thermal components, but the relative errors of the former are greater than 15% and much greater than the a few percent errors found from the spectral fitting. These errors only weakly depend on assuming an underlying spectral model for the photons, pointing to the current data being inadequate to reduce the uncertainties rather than there being a problem associated with an assumed model. The time derivative method is used to test for the presence of a 'pivot energy' in this flare. Although these pivot energies are marginally consistent with a constant value of ~ 9 keV, its values in the HXR rise phase appear to be lower than those in the decay phase. Assuming that electrons producing the high-energy component have a power law distribution and are accelerated from relatively hot regions of a background plasma responsible for the observed thermal component, a low limit is obtained for the low-energy cutoff. This limit is always lower than the break and pivot energies and locates in the tail of the Maxwellian distribution of the thermal component.

[1]School of Physics and Astronomy, SUPA, University of Glasgow, Glasgow, G12 8QQ, Scotland; j.guo@astro.gla.ac.uk

[2]Max-Planck Institute for Solar System Research, Katlenburg-Lindau, 37191, Germany

[3]Purple MountainObservatory, Nanjing 210008, China

Subject headings: Sun: flares — Acceleration of particles

1. INTRODUCTION

High-energy observations of solar flares with the Reuven Ramaty High-Energy Solar Spectroscopic Imager (RHESSI) (Lin et al. 2002) allows high resolution studies over a broad energy range from 3 keV soft X-rays to γ-rays up to 17 MeV. The photon flux in the energy range of $\sim 20 - 100$ keV can be reasonably well fitted with a power-law function, and its time-variability increases with the photon energy (Aschwanden 2005; McAteer et al. 2007). It is commonly assumed that this emission is produced by an electron population distinct from electrons forming a thermal background plasma, which is presumed to produce the low-energy X-ray emission (e.g. Aschwanden 2002). The impulsive high-energy emission originates predominantly from the chromospheric footpoints, while — at least later in the flare — the more slowly-varying low-energy emission is dominated by a hot coronal source, observed in many cases to be located near EUV flare loops (e.g. Gallagher et al. 2002). These observations are usually interpreted in the framework of the standard flare model where the hard X-ray (HXR) emission at the chromospheric footpoints of magnetic loops is bremsstrahlung of non-thermal high-energy electrons moving downward along flare loops from acceleration sites higher up in the corona (Brown 1971), with the resulting footpoint heating and evaporation leading to the hot (usually dense) coronal thermal component (Neupert 1968; Petrosian 1973; Fisher 1989). Note, we do not automatically adopt this assumed relationship between accelerated and heated particles. In fact, in Section 4, we interpret the observations in a framework where the non-thermal electrons are accelerated out of a heated thermal background. The 'non-thermal' electron distribution is usually assumed to have a low-energy cutoff, the presence of which ensures that the total electron number and power are finite. However, it is not clear that there is a theoretical mechanism for particle acceleration which can naturally lead to the low-energy cutoff distinguishing non-thermal from thermal particles (Benz 1977; Miller et al. 1997; Petrosian & Liu 2004). Indeed, it has been argued by Emslie (2003) that the low energy cutoff may be a redundant concept. Hannah et al. (2009) suggested that a sharp cutoff in the injected electron spectrum disappears with the inclusion of wave-particle interactions. A dip in the electron distribution obtained through the inversion of the observed photon spectrum of some flares may be associated with the low-energy cutoff. Kontar et al. (2008), however, showed that such a feature vanishes when isotropic albedo correction is applied.

The time correlation between the impulsive HXR and/or radio emission and the derivative of the gradual emissions at certain energies, the so-called 'Neupert effect', (Neupert

1968; Dennis & Zarro 1993) carries with it the implication that most gradual emissions are a "by-product", resulting from energy deposition by non-thermal electrons. This is also suggested by the high non-thermal electron energy content resulting from application of the standard collisional thick-target model (e.g. Emslie et al. 2004, 2005), which points to high-energy electrons forming a dominant channel in the energy conversion process. However, more quantitative examination of relevant observations show that the picture is somewhat less clear. Some flares involve heating of thermal coronal plasma in the absence of a power-law emission component (Battaglia et al. 2009), many show footpoints with impulsive phase emission within the energy range usually considered as thermal (Mrozek & Tomczak 2004), and the 'Neupert effect', which never represents a perfect correlation, does not hold in all flares or at all (thermal) energies (McTiernan et al. 1999; Veronig et al. 2002, 2005). So the possibility of heating of the solar plasma as a direct part of the energy release before and/or during the acceleration is still an open issue for investigation (Petrosian & Liu 2004; Liu & Fletcher 2009). By deriving abundances of elements with low first ionization potentials, such as calcium and iron, Feldman et al. (2004) found that at least the hot plasmas of some flares result from direct in situ heating of corona plasma, possibly due to a compression process. This approach may also lead to a measurement of the partition of hot flare plasmas originated from the corona and chromosphere.

The general question of how the pre-flare magnetic energy is converted into radiation, plasma bulk motion, thermal and non-thermal particle energy may not have a simple answer (Emslie et al. 2005). Although flares share the same kind of energy source, different flares can have quite different appearances, and possibly involve different physical processes. Nevertheless, some well-observed characteristics can still set constraints on the overall energy dissipation process. The soft-hard-soft spectral evolution of some HXR pulses is one of the most important characteristics of high-energy emissions (Kane & Anderson 1970; Grigis & Benz 2004) and may point to a turbulent particle acceleration mechanism (Grigis & Benz 2005). Early analyses (Gan 1998) suggested that there is a value of photon energy at which the non-thermal flux does not change, so that the power-law pivots about this location, a possible further model constraint. Grigis & Benz (2004) showed that there is no single 'pivot energy', rather there is a small range. Battaglia & Benz (2006) determined that in the rise phase this energy may be lower than that in the decay phase. In the context of stochastic particle acceleration from the thermal background plasma, the pivot energy should evolve with the background plasma properties (Petrosian & Liu 2004; Liu et al. 2010). However, distinguishing between different models on the basis of observations remains a challenging task (Grigis & Benz 2005).

Other constraints based on the evolution of HXR light curves include the observation that sub-second HXR pulses peak earlier in high than in low energies, consistent with a time-

of-flight dispersion if the electrons producing these pulses are accelerated at some distance from the location where the bremsstrahlung radiation is produced (Aschwanden et al. 1996a). However, this does not mean that all the energetic electrons have to be associated with these sub-second pulses. The reverse delay in the longer timescale (seconds) HXR pulses could indicate collisional escape from a coronal trap (Aschwanden et al. 1996b; Aschwanden 1998; Krucker et al. 2008), but could also be a result of a more gradual acceleration process (e.g. Bai & Ramaty 1979).

In this paper we investigate the characteristics of flare emission across a range of photon energies, and examine the association between temporal, spatial and spectral characteristics, with particular interest in the region between thermal and non-thermal parts of the spectrum. The paper is organised as follows. We first review theoretical considerations and present a simple model for the flare with an isothermal and a power-law X-ray emission component (Section 2). A simple RHESSI flare on 20th February 2002, with distinct gradual low-energy and impulsive high-energy emissions is analysed in detail (Section 3). An overview of the flare is presented in Section 3.1. The semi-calibrated photon flux is then used to derive the rate of change of photon fluxes at different energies during a prominent HXR pulse, and two temporal components are identified (Section 3.2). This is repeated in Section 3.3 but using a full spectral fit. The evolution of model parameters and the corresponding photon fluxes are used to check self-consistency of the model, and in Section 3.4 we look at the pivot energy derived from the rate of change of the photon fluxes. In Section 4, we discuss the implications of these results, and conclusions are drawn in Section 5.

2.   Thermal and Non-thermal X-ray Emission Components of Solar Flares

The impulsive phase of most flares is characterised by a monotonically increasing flux of low-energy emission and a rapidly varying flux of high-energy emission. RHESSI photon spectra are usually fitted with an isothermal component at low energies and a power-law component at high energies. For the sake of simplicity, we will ignore details of the radiative processes and assume that the observed photon flux consists of an isothermal component plus a power-law component. The photon spectrum therefore is given by

$$I(\epsilon, t) = I_{th}(\epsilon, t) + I_{nth}(t)\,(\epsilon/\mathrm{keV})^{-\gamma(t)} \tag{1}$$

where ϵ is the photon energy, $I_{th}(\epsilon, t)$ and $I_{nth}(t)(\epsilon/\mathrm{keV})^{-\gamma(t)}$ correspond to the thermal and nonthermal component, respectively. In the presence of a pivot energy ϵ_0, $I_{nth}(\epsilon_0) = I_{nth}(\epsilon_0/\mathrm{keV})^{-\gamma}$ is independent of time t and the variation of the nonthermal component is purely due to changes in the photon spectral index γ: $I_{nth}(t)\,(\epsilon/\mathrm{keV})^{-\gamma(t)} = I_{nth}(\epsilon_0)(\epsilon/\epsilon_0)^{-\gamma(t)}$.

From the spectral fitting with $I_{th}(\epsilon)$ determined from the full line-plus-continuum spectrum derived from CHIANTI (5.2) as a function of temperature T and emission measure EM, one obtains $I(\epsilon, t_0)$ at a given time indicated by t_0. The transition energy ϵ_t between thermal and non-thermal emissions, where the photon fluxes produced by the corresponding electron populations are equal, is determined by $I_{th}(\epsilon_t, t_0) = I_{nth}(t_0)(\epsilon_t/\mathrm{keV})^{-\gamma(t_0)}$, where I_{nth} and γ are fitting parameters.

The normalized time rate of change of the photon flux at a given energy ϵ is given by

$$R(\epsilon, t) \equiv \frac{dI(\epsilon, t)}{I(\epsilon, t) \cdot dt} = \frac{\dot{I}_{th}(\epsilon, t) + \dot{I}_{nth}(t)(\epsilon/\mathrm{keV})^{-\gamma} - I_{nth}(t)\dot{\gamma}(t)\ln(\epsilon/\mathrm{keV})(\epsilon/\mathrm{keV})^{-\gamma}}{I_{th}(\epsilon, t) + I_{nth}(t)(\epsilon/\mathrm{keV})^{-\gamma(t)}} \quad (2)$$

$$\approx \begin{cases} R_{th} \equiv \dot{I}_{th}(\epsilon, t)/I_{th}(\epsilon, t) & \text{for} \quad \epsilon \leq \epsilon_t \\ R_{nth} \equiv \dot{I}_{nth}(t)/I_{nth}(t) - \dot{\gamma}(t)\ln(\epsilon/\mathrm{keV}) & \text{for} \quad \epsilon > \epsilon_t \end{cases} \quad (3)$$

where the dot above the relevant quantities indicates the derivative with respect to time and we have used the fact that the thermal and nonthermal components dominate the low- and high-energy photon spectra, respectively, to derive the approximate expression. The rate of change of photon flux of the thermal and power-law component are indicated by R_{th} and R_{nth}, respectively. In the RHESSI energy range we consider, the thermal continuum spectrum always dominates at low energies and the free-free thermal bremsstrahlung emission is proportional to $EM(t)/\left\{\epsilon\, T(t)^{1/2}\exp[\epsilon/k_\mathrm{B}T(t)]\right\}$, where $EM(t) = n_{th}^2 V$ and V and n_{th} indicate the source volume and density of the thermal electrons respectively. k_B is the Boltzmann constant.

$$R_{th} = \frac{\dot{I}_{th}(\epsilon, t)}{I_{th}(\epsilon, t)} = \frac{\dot{EM}(t)}{EM(t)} + \frac{\epsilon\dot{T}}{k_\mathrm{B}T^2} - \frac{\dot{T}}{2T}. \quad (4)$$

Inclusion of emission lines and free-bound emission will introduce correction terms to this equation.

In principle, one can obtain the right-hand side of Equation (2) from the spectral fits. The left-hand side can be obtained from light curves of different energy bands directly. If the photon spectral model given by Equation (1) is sufficient, Equation (2) should be satisfied. If the change in the temperature of the thermal component is small, then the rate of change of the photon flux is independent of the photon energy ϵ in the thermally-dominated energy range (Eq. 4). One can therefore obtain R_{th} by fitting the rate of change of photon flux in the thermal regime with a function independent of ϵ. There will be an energy ϵ_t', where the time derivatives of thermal and non-thermal components are equal, i.e. $R_{th} = R_{nth}(\epsilon_t')$ and if the simple equivalence between non-thermal/thermal emission and impulsive/gradual emission holds then ϵ_t' should be comparable to ϵ_t obtained from spectral fits. Equation (2) also provides a means to investigate the presence of a constant 'pivot' energy ϵ_0 for the

power-law component, which will occur where R_{nth} goes to zero - the invariant point in the photon spectrum of the power-law component.

3.   Observations

RHESSI observed a flare on 20th February 2002 in the NOAA active region 9825, located near the northwest limb of the Sun at N16W80 ($919''$W, $285''$N) a few days after its successful launch on 5 February 2002. It is the focus of several earlier studies dealing with the characteristics during the HXR peak (Sui et al. 2002; Aschwanden et al. 2002). The imaging and spectroscopic software has been improved significantly since then and the instrumental response is better understood and incorporated in the RHESSI software packages. We choose this event because of the very simple shape of its light curves, and present an investigation here emphasizing the relationship between the low-energy and high-energy emission components.

3.1.   Light curves, Images, and Spectra

This GOES 1-8 Å C7.5 flare exhibits a prominent HXR pulse lasting for about 50 seconds with count rates above 12 keV peaking near 11:06:20 UT. The first three panels of Figure 1 show a summary of GOES and RHESSI observations of this flare. The 3-6 keV light curve shows some impulsive behavior, while the 6-12 keV counts are relatively smooth. The RHESSI attenuator state during this flare was A1. Counts in the 3-6 keV channel when the attenuators are in place are almost all from higher energy photons above 11 keV, because of the effect of K-escape (Smith et al. 2002). We therefore only analyze counts above 6 keV in this work. The attenuator also reduces the count rate at low energies significantly leading to a livetime better than 93% for all the detectors. Pulse pileup can then be ignored in the spectral study (Smith et al. 2002). The rise of the RHESSI count rates below 25 keV becomes evident after 11:04 UT marking the onset of the flare. The slowly rising count rates before 11:04 UT are likely caused by particle events as is evident from the gradual varying count rates in higher energy channels where the statistical errors are significant. The background profile can be subtracted with sufficient accuracy by modeling this gradual varying component in different energy channels separately.

The fourth and fifth panels of Figure 1 show the GOES temperature and emission measure, respectively. The background fluxes in the two energy channels are chosen as a linear interpolation between average fluxes during two intervals before and after the flare and
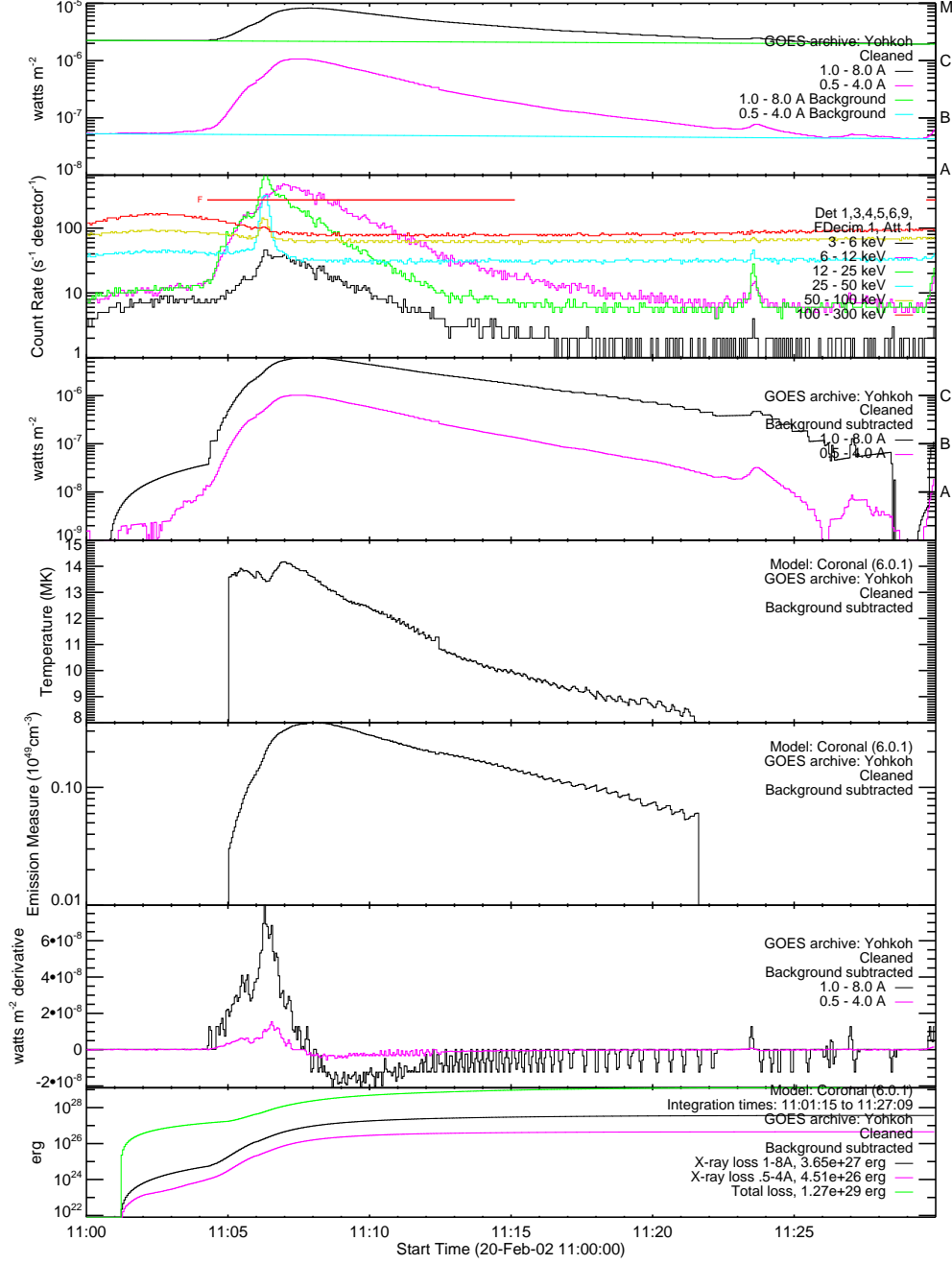
Fig. 1.— Summary of RHESSI and GOES observations. The high-lightened range shows the time interval (11:05:50 —11:06:50) used for images and spectra in Figures 2 and 3. The top panel shows the soft X-ray (SXR) lightcurves and chosen backgrounds (as linear interpolation of fluxes of two intervals before and after the flare) for both energy bands observed by GOES. The second panel shows the RHESSI count rate in several energy bands. The third panel shows GOES lightcurves with the background subtracted. The fourth and fifth panels show, respectively, the temperature and emission measure derived from the GOES fluxes, in agreement with results obtained by Sui et al. (2002). The sixth panel shows the time-derivatives of the GOES lightcurves, which is qualitatively correlated with the HXR count rates in the top panel. The bottom panel shows the energies radiated by the

are shown in the first panel. The temperature and emission measure can not be obtained before 11:05 UT, presumably due to the relatively low background subtracted fluxes shown in the third panel. The values obtained for the impulsive phase are rather insensitive to the background selection. These results are in agreement with those obtained by Sui et al. (2002) for the prominent HXR pulse. We note that the temperature does not change significantly throughout the rise phase of the 6-12 keV count rate from 11:05 to 11:07 UT. The emission measure appears to grow exponentially at the beginning with a growth time of ~ 40 seconds, and the growth rate decreases significantly after the HXR pulse. The sixth panel shows the time derivatives of the GOES fluxes. Although these derivatives peak near the peak of the HXR pulse, and a secondary peak before the major peak appears to be correlated with RHESSI light curves below 25 keV in rough agreement with the Neupert effect, a broader correlation is not very obvious. Since the first peak does not contain high energy (> 25 keV) emissions which normally have a longer decay time than lower energies, we assume that the two peaks are independent and the first peak does not significantly affect the spectral properties determined for the major one. The bottom panel shows the radiative energy produced by the isothermal source, obtained by fitting the GOES fluxes using CHIANTI 6.0.1 and assuming coronal abundances (Dere et al. 2009). The total radiated energy from the hot plasma is about 10^{29} ergs for this flare.

The right panel in Figure 2 shows the source structure at several energies during the prominent HXR peak from 11:06:10 to 11:06:30 UT obtained using the Pixon algorithm (Pina & Puetter 1993). The weak HXR coronal source near the solar limb has been interpreted as the site of particle acceleration by Sui et al. (2002). Aschwanden et al. (2002), on the other hand, inferred a much smaller loop. Our results suggest that both large and small loops are present at energies up to 25 keV. There are also clear footpoints at > 25 keV which appear to be at the end of the lower energy loops. This imaging does not support the suggestion by Sui et al. (2002) that there is an independent low-energy thermal source between the two HXR footpoints, rather it indicates that the small loop connects to the HXR footpoints. The structure just before the flare peak is shown in the left panel of Figure 2.

The time evolution of X-ray sources at 6-9 keV, 9-12 keV, and 12-25 keV are shown in Figure 3. The 6-9 keV source structure (in the left panel) is relatively simple, loop-like and compact before the HXR pulse. It becomes more extended in the following two time intervals and develops three sub-sources (though there is a possibility that this is over-resolution by the Pixon algorithm). The 9-12 keV emission is primarily loop-like but more extended than its 6-9 keV counterparts. Features associated with the footpoints start to emerge. The distinction between footpoint sources and loop source(s) becomes very ambiguous at 12-25 keV (in the right panel of Figure 3). The brightest locations are associated with the footpoints at the
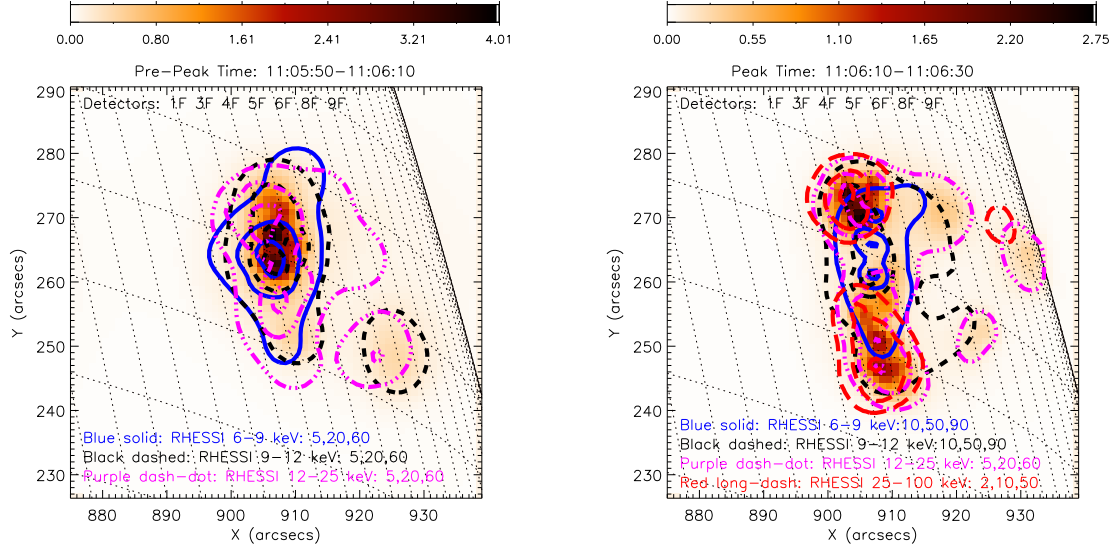
Fig. 2.— Images of the flare for a 20 second interval before (Left) and a 20 second interval during (right) the HXR peak. The map color is in the unit of photons cm^{-2} s^{-1} $arcsec^{-2}$. *Left:* The image and dashed contours (5, 20, and 60 % of the peak brightness) are for 9-12 keV energy band. The solid (5, 20, and 60 %) and dash-dot (5, 20, and 60 %) contours are for the 6-9 keV and 12-25 keV energy band, respectively. *Right:* The image and dot-dash contours (5, 20, and 60 %) are for the 12-25 keV energy band. The solid (10, 50, and 90 %), dashed (10, 50, and 90%) and long-dash (2, 10, 50%) contours are for the 6-9 keV, 9-12 keV and 25-100 keV energy band, respectively.
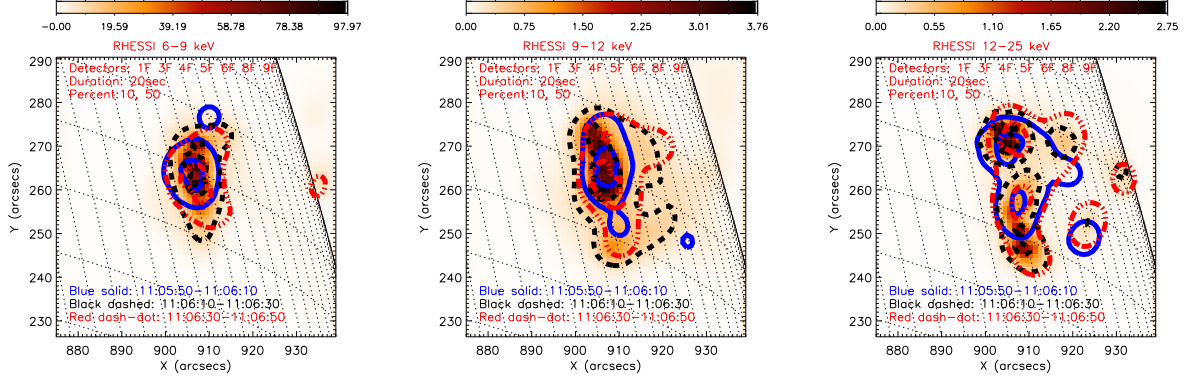
Fig. 3.— Evolution of the X-ray images at 6-9 keV (left), 9-12 keV (middle), and 12-25 keV (right). The map color is in the unit of photons cm^{-2} s^{-1} arcsec^{-2}. The image and dashed contours (10, 50%) are for the interval of the HXR peak. The solid contours and dash-dot contours are for the interval before and after the HXR peak, respectively.

HXR peak, but the 12-25 keV structure is elongated (as is the 9-12 keV source in the middle panel) and may include a loop component. The X-ray images therefore reveal a complicated pattern of low and high energy sources, with no clear distinction between footpoints and loop at energies from ∼10 to 25 keV.

Figure 4 shows the photon spectra fitted with an isothermal plus a power-law component for the three 20-second intervals of Figure 3. For this preliminary study, the RHESSI background is chosen as a linear interpolation, made between the average counts during the intervals 11:01:58 - 11:02:38 and 11:20:38 - 11:21:18. More detailed modeling of the background is carried out in Section 3.3, where the spectra for 4-second intervals are analyzed. (Although we choose a broken power-law model in the fitting, the break energy is fixed at 5 keV which is below the energy range of the data.) The soft-hard-soft spectral evolution is evident with the photon spectral index varying from 4.1 to 3.4 and to 5.5. The emission measure and temperature are $EM = 4.7 \times 10^{47}$ cm^{-3}, kT =1.5 keV; $EM = 9.9 \times 10^{47}$cm^{-3}, kT =1.4 keV, and $EM = 1.6 \times 10^{48}$ cm^{-3}, kT =1.3 keV, respectively. The emission measure is slightly lower and the temperature is slightly higher than those from the GOES spectral fit, which may be attributed to the different energy ranges covered by these two instruments. Comparison of these spectra shows that the 12-25 keV emission is more and more dominated by the power-law component as the flare evolves. The spectral fit of the last interval has also the highest values of reduced χ^2 (1.37) and residuals, leading to a probability of 8% to get a larger χ^2 assuming a correct model. Indeed, for the last interval a thermal plus a broken power-law model gives much improved spectral fit. We also study the spectral evolution
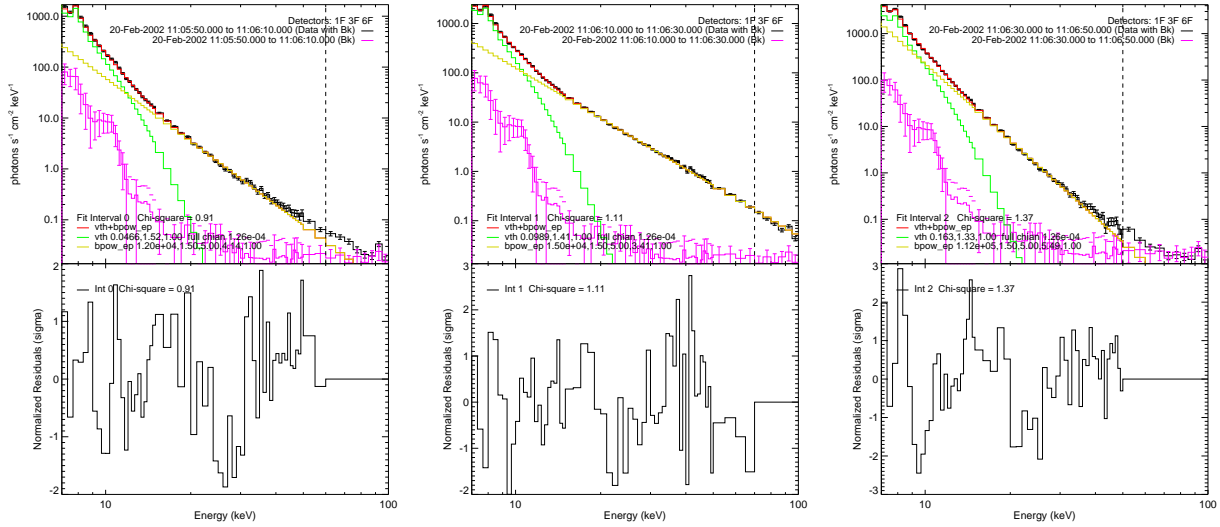
Fig. 4.— Photon spectra of the three 20-second intervals in Figure 3 fitted with an isothermal plus a power-law model. Time starts from 11:05:50 and increases from left to right. Model parameters are indicated in the figure.

after the impulsive phase. The simple thermal plus a single power-law model can be ruled out by the relatively softer high-energy spectra, which imply dominance of very low-energy emission by the power-law component. A thermal plus a broken power law or multi-thermal model can give acceptable fit. However, one should note that the high-energy photon fluxes change dramatically during the two intervals before and after the HXR peak and the large systematic residuals around the iron-line complex at 6.7 keV indicate that this feature has not been modeled properly. Currently, the only way to improve the modeling of emission lines is to fit spectra from individual detectors and take into account small gain changes and pulse pile up, which is beyond the scope of the current investigation.

3.2. Semi-calibrated light curves and their rate of change

We here study the photon flux change rate $R(\epsilon, t)$ given by Equation (3) to quantify the rate of change of photon flux — how impulsive or gradual the event is — as a function of both energy and time. We do this first in a model-independent way using the semi-calibrated photon flux. Semi-calibrated photon fluxes can be obtained from the observed count rates by using the diagonal elements of the spectral response matrix. Although the photon flux obtained this way does not take into account the full spectral response matrix of RHESSI, it can be readily obtained and gives an approximate description of the photon flux from
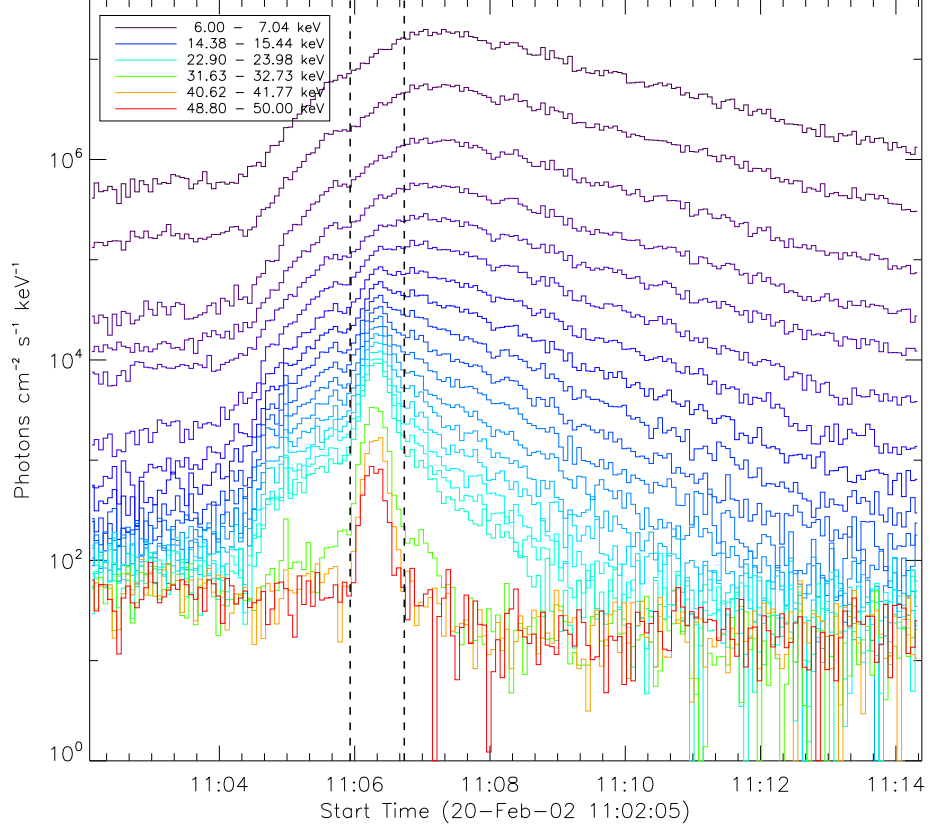
Fig. 5.— Semi-calibrated photon flux $f(\epsilon, t)$ of the flare averaged over 4 s intervals. The curves with different colors represent photon counts in 40 different energy bands from 6 to 50 keV. The vertical dash lines represent the start (11:05:56) and end time (11:06:44) of the HXR pulse. Notice that not all of the 40 energy bands are shown.
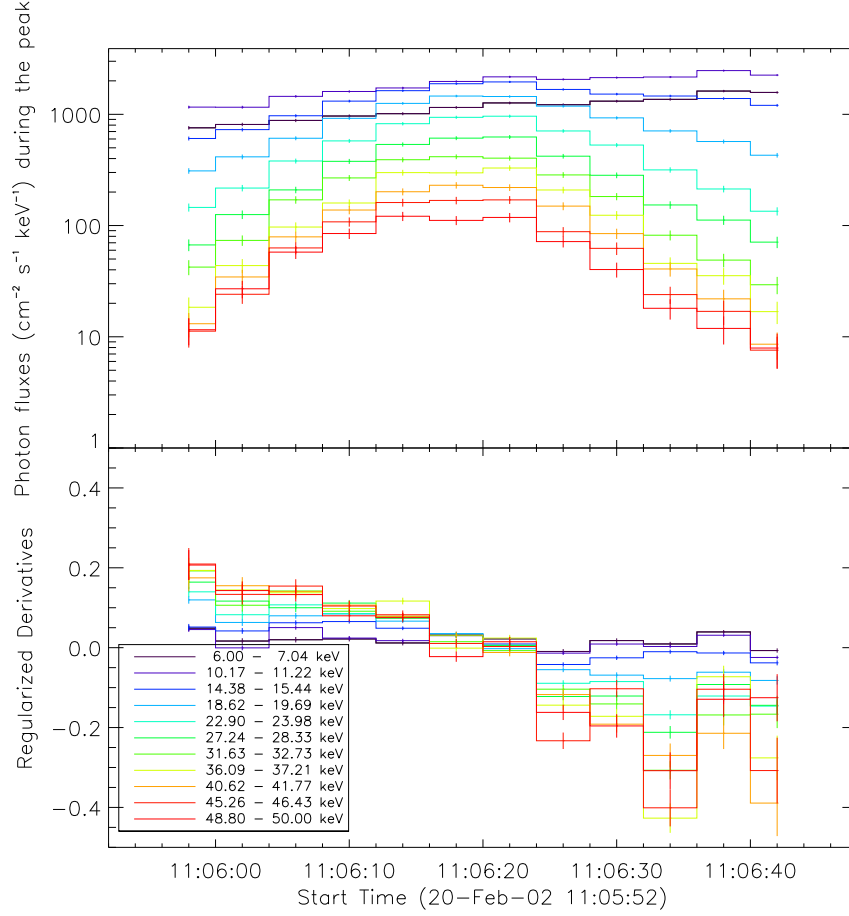
Fig. 6.— *Top*: Semi-calibrated photon flux $f(\epsilon, t)$ and its $\pm 1\sigma$ statistical errors during the HXR pulse (11:05:56—11:06:44). *Bottom*: The rate of change of the photon flux $R(\epsilon, t) = df(\epsilon, t)/dt/f(\epsilon, t)$ (s^{-1}) and its corresponding $\pm 1\sigma$ errors calculated with the regularized method. Notice that we have shown only 11 out of the 40 energy bands.
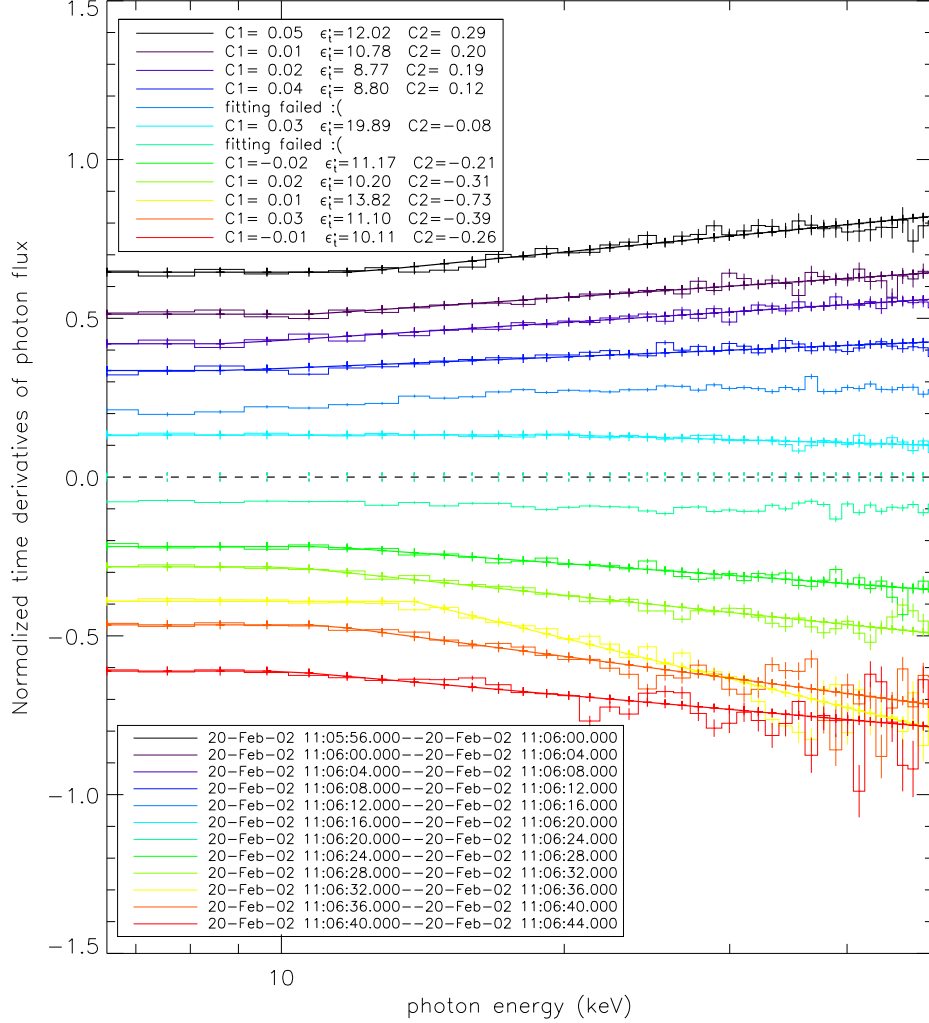
Fig. 7.— Rate of change of semi-calibrated photon flux $R(\epsilon, t) = df(\epsilon, t)/dt/f(\epsilon, t)$ (s^{-1}) versus the photon energy for 12 4-second time bins. The error bars give $\pm 1\sigma$ uncertainties. The data are fitted with the model described by Equation (5) and the best fit models are shown as solid lines. For illustrative purpose, the lines are shifted vertically by the values of [0.6, 0.5, 0.4, 0.3, 0.2, 0.1, -0.1, -0.2, -0.3, -0.4, -0.5, -0.6] in time sequence. The fit does not converge for the fifth and seventh time intervals. The model parameters C1, ϵ_t and C2 of the fit are indicated in the legend.

the source, and one which does not depend on assuming a particular form of the photon spectrum (note, we investigate full spectral fitting in Section 3.3). Following the arguments of Section 2, with the photon spectrogram obtained this way, one can test whether the two components identified from spectral fits are compatible with the two temporal components.

Figure 5 shows some of the detailed semi-calibrated photon fluxes $f(\epsilon, t)$ in forty energy bands between 6 and 50 keV. Each energy bin is set to be no smaller than 1 keV which is the energy resolution of RHESSI (Smith et al. 2002). The vertical axis indicates the photon flux averaged over a 4 second interval in the corresponding energy band. The background fluxes of high energy bands decrease gradually with time. We model these background fluxes for different energy bands with a first order polynomial fitting of background values obtained before and after the HXR pulse.

We use the regularized method developed by Kontar & MacKinnon (2005) to obtain the time derivatives of these light curves. This method gives smoother derivatives while avoiding large errors, typical of finite differences of discrete numerical data. We assume statistical error for the photon flux $\sigma f(\epsilon, t) = M^{-1}(\epsilon) \, C(\epsilon, t)^{1/2}$ where M is the diagonal components of the instrument response matrix and C is the count rate. The top panel in Figure 6 gives the photon flux $f(\epsilon, t)$ and its 1σ statistical error $\sigma f(\epsilon, t)$ in different energy bands during the HXR pulse. The bottom panel shows the rate of change of photon flux $R(\epsilon, t) = df(\epsilon, t)/dt/f(\epsilon, t)$ and its 1σ error $\sigma R(\epsilon, t)$, which is the standard deviation of $R(\epsilon, t)$ modeled with a Gaussian by sampling 5000 points in $df(\epsilon, t)/dt$ and $f(\epsilon, t)$ within their respective 1σ range of a Gaussian distribution. Here only the 1σ range of a Gaussian distribution is sampled for the following reason. The relatively low flux f and its relatively large 1σ error mean that a sampling over the full distribution will have points with $f(\epsilon, t)$ close to zero. This will lead to very high values of $R(\epsilon, t)$, whose distribution is poorly fitted with a Gaussian. The 1σ error obtained this way should be considered as a lower limit. The photon fluxes at lower energies have a more gradual temporal evolution and lower rate of change, in contrast to the high-energy band photon fluxes, which have rapid rise and decay phases and highly variable rate of change. The absolute value of the rate of change often increases with the photon energy. However, the 1σ error of the rate of change of photon flux also increases with energy, and the variation in the rates of change at high energies may not be significantly different from those at low energies. At the time bin for the peak from 11:06:20 to 11:06:24, however, the rates for all energies are around zero.

Figure 7 shows the energy dependence of the rate of change of photon flux at different 4 second time intervals of the HXR pulse. It is clear that the higher energy fluxes have higher values of the derivative in the rise phase (before 11:06:20) and lower values of the derivative in the decay phase (after 11:06:24). This confirms that higher energy fluxes are

more variable than those at low energies. There appears to be two temporal components. At low energies, the rate of change is nearly independent of the photon energy. At high energies, the energy dependence of the rate of change appears to increase linearly with the logarithm of the photon energy. To quantify these results, we adopt the following model for the rate of change R

$$R = \begin{cases} C1 & \text{for} \quad \epsilon \leq \epsilon_t' \\ C1 + C2 \log_{10}(\epsilon/\epsilon_t') & \text{for} \quad \epsilon > \epsilon_t'. \end{cases} \tag{5}$$

There are therefore three model parameters: C1, C2, and ϵ_t'. The solid lines in Figure 7 indicate the best-fit model (using the curvefit function in IDL). Note that the 4th and 7th time intervals are not fitted with the model due to significant uncertainty in ϵ_t' because of low values of the rate of change of photon flux at all energies near the HXR peak.

A comparison of equations (3) and (5) shows that

$$C1 \quad = \quad R_{th} = \dot{EM}(t)/EM(t), \tag{6}$$
$$C2 \quad = \quad -\ln 10 \cdot \dot{\gamma}, \tag{7}$$

where we have assumed that the temperature of the thermal component does not change during the HXR pulse (demonstrated using spectral fitting in the next Section). ϵ_t' is the transition energy, where the rate of change of the high and low energy components are equal: $R_{th} = R_{nth}(\epsilon_t')$. If the isothermal and power-law model of equation (1) indeed gives sufficient description of the observations, ϵ_t' should be comparable to the transition energy identified from the spectral fit ϵ_t.

3.3. Spectral fit and the rate of change of photon flux and model parameters

The semi-calibrated photon flux, which is simple and fast to obtain, may give a sufficient approximation of the photon flux from the source at high photon energies, but the non-diagonal elements of the response matrix become important at low energies. By carrying out a full spectral fit, which is much more time-consuming, and determining the model parameters from this, we can check for consistency with the results based on the semi-calibrated flux. With the spectral fitting package OSPEX, the spectrum of counts from 6 to 60 keV are fitted with an isothermal plus a single power-law model for time bins of 4 seconds from 11:05:56 to 11:06:44 UT. Note that the model of CHIANTI (5.2) rather than CHIANTI (6.0.1) used in GOES data is applied here due to the lack of implementation of the newer model in OSPEX. Due to the change of background fluxes in both time and energy, the background is separately selected for five different energy bands(3 to 6 keV, 6 to
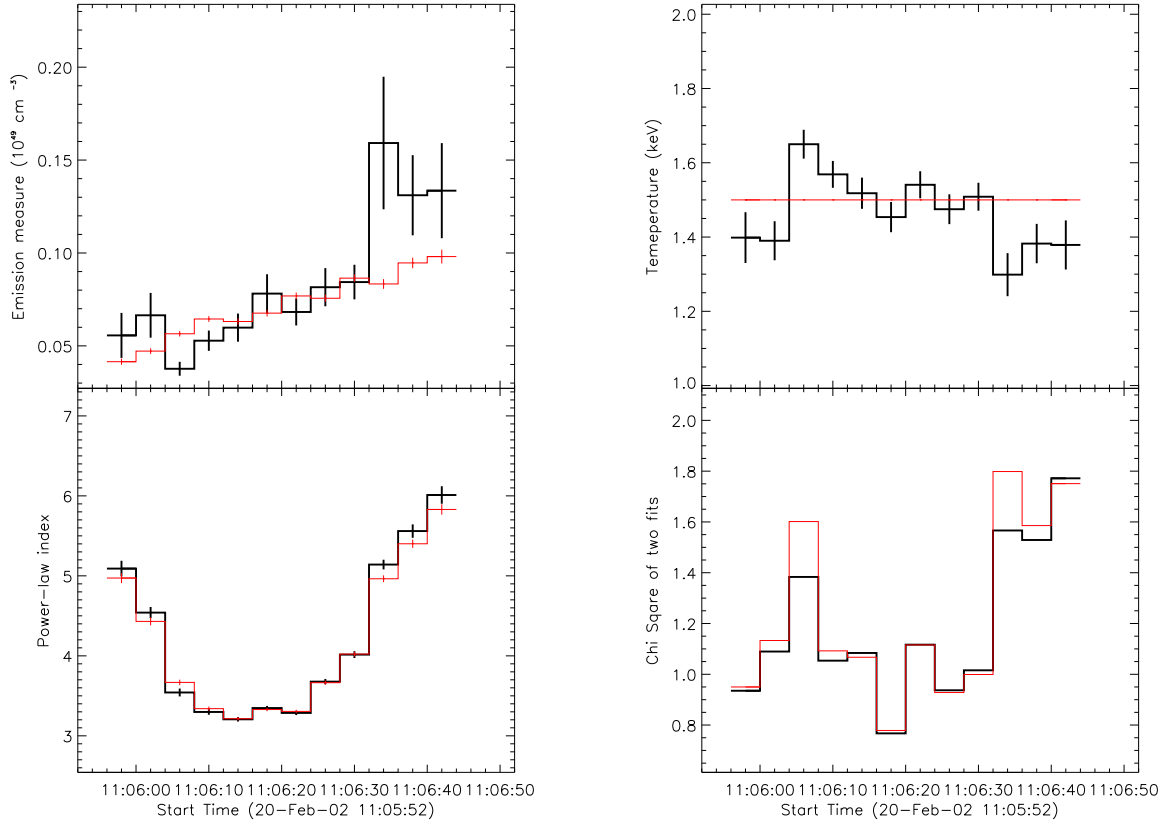
Fig. 8.— Parameters of an isothermal plus a single power-law spectral fits with temperature adjustable (thick black lines) and temperature fixed at 1.5 keV (thin red lines). The top-left, top-right, bottom-left, bottom-right panels show the emission measures, temperatures, the power-law spectral indexes, and the χ^2 of both fits, respectively.
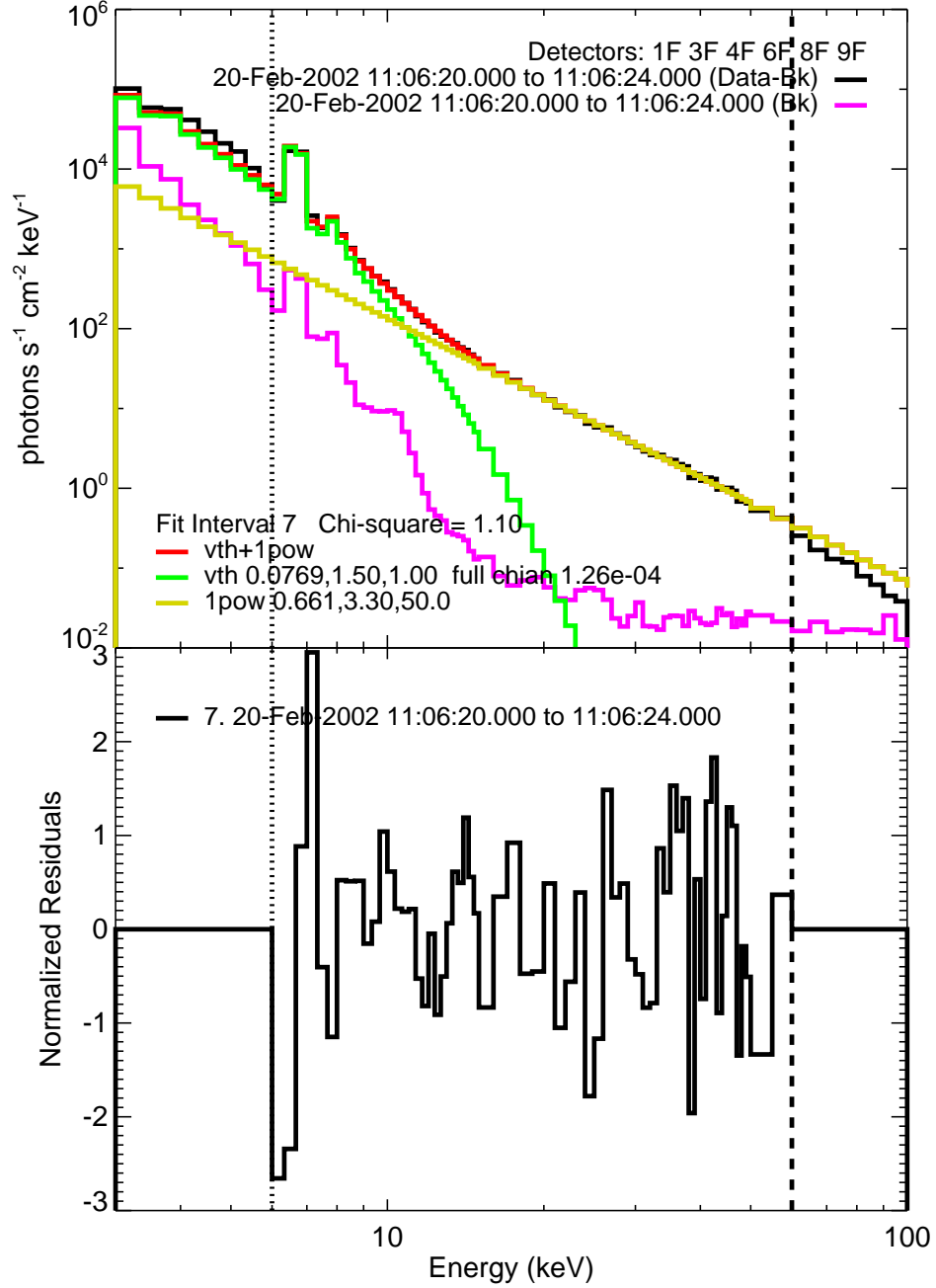
Fig. 9.— Top panel: photon flux spectrum for the peak time interval: 11:06:20 to 11:06:24. The magenta line shows the background and the black line is the photon data with background subtracted. The spectrum of data from 6 to 60 keV is fitted with an isothermal plus a single power-law model. The green line represents the thermal model and the yellow line is for the power-law model. The red line is for the total thermal plus power-law spectrum. Bottom panel: normalized residuals of the spectral fit.

12 keV, 12 to 25 keV, 25 to 50 keV and 50 to 100 keV) both before and after the flare and fitted with the first order polynomial. [1] Since we are mostly interested in a relatively low energy range, where the transition between the high and low energy component occurs, an upper energy bound of 60 keV is chosen to avoid potential spectral steepening at even higher energies (Sui et al. 2002) and to ensure adequate counts above background throughout the period of interest. Aschwanden et al. (2002) also fitted the spectra of this flare with a single power-law from 15 to 50 keV.

We first fit with the temperature, emission measure, power-law index and normalization of the power-law component as free parameters. The results are indicated by the black lines in Figure 8. Both the emission measure and power-law index show significant variation during the HXR pulse. The variation of the temperature, however, is relatively small, between 1.3 and 1.7 keV. To facilitate comparison with the theoretical model, we then fix the temperature at a typical value of 1.5 keV and do the spectral fit again. The results are indicated by the red lines in Figure 8. From the χ^2 of the bottom right panel, we conclude that this model gives a fit to the observations which is as good as that in the model having the temperature as a free parameter. The smaller number of free parameters also gives smaller uncertainties for other model parameters, and the emission measure (top-left panel) has a smoother evolution when the temperature is fixed. The power-law spectral indices (bottom-left panel) from both fits are almost identical and both have a soft-hard-soft evolution. The goodness of the spectral fitting is evaluated by the reduced χ^2 which is shown in the bottom-right panel. The χ^2 for both fits are very similar except during one rise time bin (11:06:04 to 11:06:08) and one decay time bin (11:06:32 to 11:06:36).

For the sake of simplicity, in the following we only use results obtained with the model temperature fixed at 1.5 keV. Figure 9 shows the photon spectral fit with the thermal plus power-law model for the peak time bin (11:06:20 to 11:06:24). The emission measure is $7.69 \pm 0.18 \times 10^{47} \mathrm{cm}^{-3}$. The normalization of the power-law component at 50 keV is 0.66 ± 0.01 photons $\mathrm{s}^{-1}\mathrm{cm}^{-2}\mathrm{keV}^{-1}$. The power-law spectral index is 3.3 ± 0.02. The normalized residuals are shown below the spectrum. The residuals are between -3 and 3 with slightly larger values at 6-7 keV where the iron emission lines locate. To model this feature correctly, one needs to fit spectra from individual detectors and take into account small gain changes

---

[1]The time intervals chosen for fitting the background fluxes are 11:01:52 - 11:02:56 and 11:21:00 - 11:21:56 for 3 - 6 keV, 11:02:00 - 11:02:56 and 11:19:56 - 11:21:00 for 6 - 12 keV, 11:01:56 - 11:02:32 and 11:18:04 - 11:19:00 for 12 - 25 keV, 11:04:08 - 11:04:24 and 11:11:12 - 11:13:16 for 25 - 50 keV, and 11:04:20 - 11:04:48 and 11:08:04 - 11:09:04 for 50 - 100 keV. We also modeled the background fluxes for eleven energy bins from 3 to 100 keV using a third order polynomial fit with six intervals chosen around the peak time and obtained very similar spectral results.

and pulse pile up. We focus on the transition between thermal and nonthermal components here and leave this caveat for a future investigation.

With the forward-fitted photon fluxes f obtained above, we calculated the normalized rate of change $R(\epsilon, t) = (df(\epsilon, t)/dt)/f(\epsilon, t)$ with the same regularized method as was used on the semi-calibrated photon fluxes. Figure 10 shows the energy dependence of the rate of change with different colors representing different time bins. The errors are large for high energies because the photon fluxes at high energies are low and their relative errors are big. The solid lines are the model fit shown in Eq. (5). Notice that the 5th and 7th lines are again not fitted with the model.

According to Eqs. 6 and 7, the rate of change of the $EM(t)$ and $\gamma(t)$ can be obtained directly from the semi-calibrated photon flux, and from the spectral fits with the regularized method for derivatives (Kontar & MacKinnon 2005). Figure 11 compares the rate of change of the emission measure and the power-law spectral index with the above three methods: first with the semi-calibrated data (see Figure 7), second with the photon flux derived from spectral fit (see Figure 10), and third directly from the evolution of these parameters determined in the spectral fit (see Figure 8). One can see that these rates obtained with different methods are consistent. The rate of change of the emission measure is positive in most of the time bins. This indicates that the thermal emission is increasing nearly monotonically during the HXR pulse. The time evolution of $\dot{\gamma}$ is also consistent with the soft-hard-soft evolution. The regularized method provides a powerful means to quantify this behavior.

3.4. Transition and Pivot energy

With the results obtained above, one can check the consistency of the model given by Equation (1) and test whether there is one pivot energy ϵ_0 for the duration of the whole HXR pulse. The transition energy between the two temporal components ϵ'_t and between the two spectral components ϵ_t should be comparable if the two spectral components have distinct energy and time dependences, as expected. For results obtained with the spectral fitting in Section 3.3, good spectral fits will guarantee that ϵ'_t be comparable to ϵ_t. However, with the semi-calibrated data, these two transition energies characterized the spectral evolution in two distinct dimensions. There is no guarantee that the two spectral components will match the two temporal components self-consistently. The top panel of Figure 12 shows ϵ_t and ϵ'_t obtained from the analyses above. ϵ_t has a relative error of a few percent and varies between 10 and 12 keV, which is consistent with a constant value of ~ 11 keV. Although ϵ'_t varies in a larger energy range of 8 to 20 keV, the relative errors are greater than 15% and its values are also consistent with a constant of ~ 11 keV. The agreement of these quantities
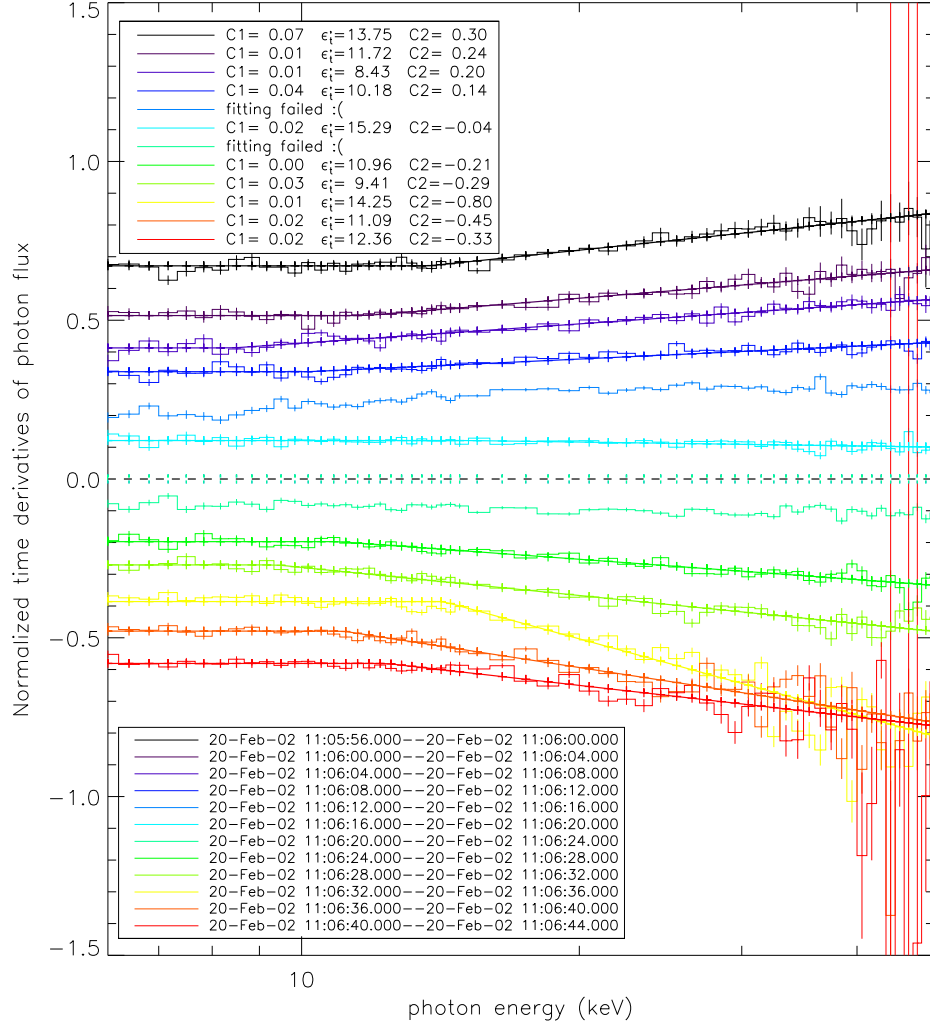
Fig. 10.— Same as Figure 7 ($R(\epsilon, t)$ in s^{-1}) but for the photon flux derived from spectral modelling.
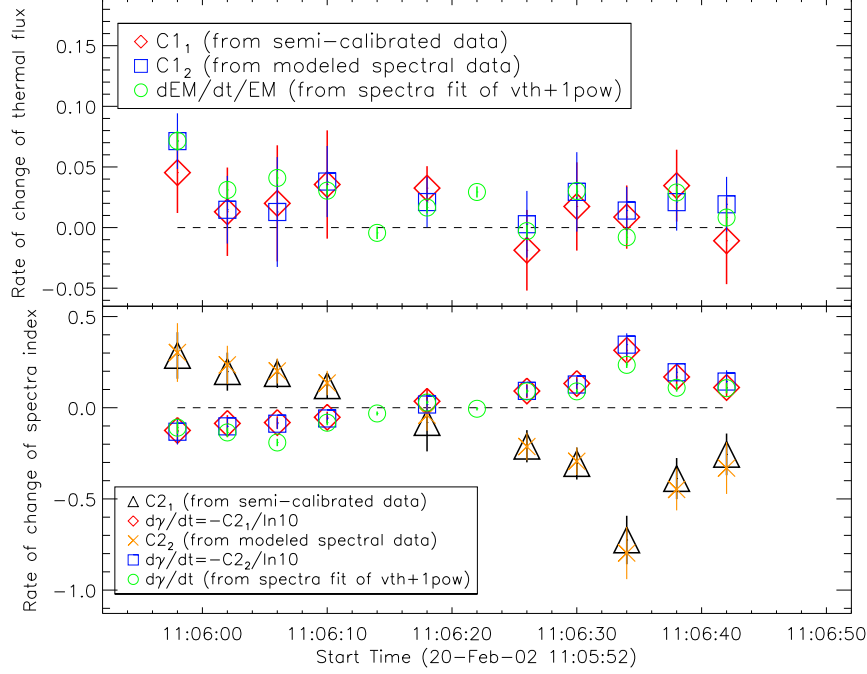
Fig. 11.— *Top panel*: comparison of the rate of change of low-energy photon flux $C1_1$ (red diamonds) derived with the semi-calibrated data, $C1_2$ (blue squares) with the modelled spectral data, and the rate of change of the emission measure $\dot{EM}/EM$ (green circles). *Bottom panel*: comparison of parameters $C2_1$ (black triangles) and $C2_2$ (orange crosses) derived with the semi-calibrated data and modelled spectral data respectively. The rate of change of the spectral index $\dot{\gamma}$ can be obtained from $C2_1$ and $C2_2$ as shown in the legend. Red diamonds, blue squares and green circles represent $\dot{\gamma}$ from semi-calibrated photon fluxes, from modelled spectral photon fluxes, and from the time derivatives of the power-law index respectively. Error bars of $\dot{EM}/EM$ and $d\gamma/dt$ (both in green circles) are obtained with the regularized method. Error bars of all the other parameters indicate the 1σ uncertainties of curve fit in Figures 7 and 10 and described by Eq. (5).
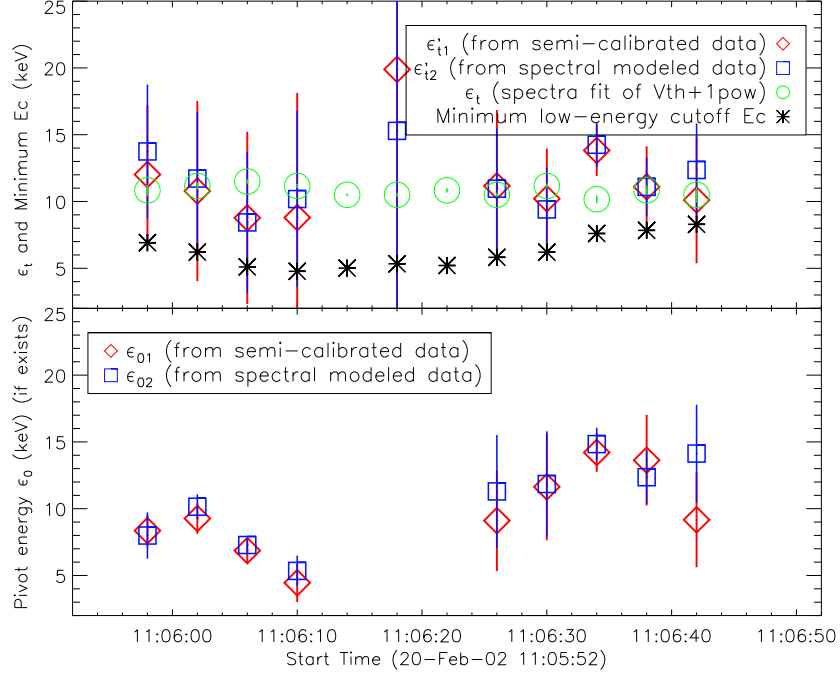
Fig. 12.— *Top panel*: evolution of the transition energy between the low and high energy component derived from variability of the semi-calibrated data (red diamonds), the modelled spectral data (blue squares) and from the isothermal plus power-law spectral fit (green circles). The error bars of ϵ'_{t1} and ϵ'_{t2} show, respectively, the uncertainties of curve fit in Figures 7 and 10 as described by Eq. (5). The error of ϵ_t is the standard deviation of 5000 simulated intersections between thermal and nonthermal components taking into account uncertainties of all the spectral fitting parameters. Also shown is the possible minimum electron low-energy cutoff E_c (Section 4). *Bottom panel*: pivot energy ϵ_0 with 1σ errors (see Section 3.4 for more details) derived from the variability of the semi-calibrated data (red diamonds) and modelled spectral photon fluxes (blue squares).

implies consistency of the model. The big error bars of ϵ'_t are due to the uncertainty of determining the cross point of the two lines in the fitting shown in Figures 7 and 10. This may reveal a complicated physical process where the transition between the slow-varying gradual component and the impulsive component is rather an energy range than a single point.

The usual method of determining ϵ_0 by spectroscopic fitting depends on the assumed spectral model. We instead use the above rate of change study to derive ϵ_0 and its errors for each interval. From equation (5), one can show that the rate of change of the photon flux of the power-law component is zero at

$$\epsilon_0 = \epsilon'_t \cdot 10^{-C1/C2} . \tag{8}$$

This is the pivot energy at a given time interval. With parameters $C1$, $C2$, and ϵ'_t obtained above, we calculated the pivot energy ϵ_0 as shown in the bottom panel of Figure 12. The error of ϵ_0 is taken as the standard deviation of simulated ϵ_0 with 5000 sampling points of ϵ'_t, $C1$, and $C2$ distributed within their respective 1σ range of a Gaussian distribution. The results are consistent with a constant value of ~ 9 keV except for the fourth and tenth intervals where deviations of ϵ_0 from 9 keV are greater than 3σ. These values of the pivot energy are also less than those obtained by Battaglia & Benz (2006) for the loop top source of a few other flares, but are in agreement with these of the footpoint sources especially for values in the HXR decay phase. Since $C1$ is mostly positive and $C2$ evolves from positive to negative values from the HXR rise to decay phase, $10^{-C1/C2}$ evolves from less than 1 to greater than 1, implying that ϵ_0 increases from $\lesssim \epsilon'_t$ to $\gtrsim \epsilon'_t$. It should be noticed that when $C2$ approaches zero, the amplitude of $C1/C2$ approaches infinity and $10^{-C1/C2}$ approaches either 0 or infinity, both of which are not physical. It also leads to huge error bars for time bins near and after the HXR peak. Indeed, a sampling of $C2$ over a full Gaussian distribution after the peak (when $C2 < 0$ and $C1 > 0$) will lead to infinite values of ϵ_0, whose distribution is poorly fitted with a Gaussian. Theoretically, for HXR pulses with soft-hard-soft spectral evolution, if the transition energy and temperature do not change significantly and the emission measure has a gradual and monotonic increase, the pivot energy in the decay phase should be higher than that in the rise phase, as indicated in Figure 12. This result is in agreement with previous studies (Grigis & Benz 2005; Battaglia & Benz 2006) and may be attributed to an effect of chromospheric evaporation (Liu et al. 2010). The pivot energy ϵ_0 is also comparable to the transition energies ϵ_t and ϵ'_t, in agreement with the scenario where energetic electrons are accelerated from a low-energy thermal background plasma (Benz 1977; Petrosian & Liu 2004; Grigis & Benz 2006).

4. Discussion

We started with the hypothesis that there are two distinct emission components with low energy photons evolving gradually and high energy photons having a rapid evolution. One consequence of this is that, as long as the temperature of the thermal component varies slowly (much slower than the emission measure), which simplifies the model significantly [see eq. (4)], the break energy between non-thermal and thermal emission in the photon spectrum should be comparable to the transition energy between slowly- and rapidly-varying photon fluxes found by evaluating time derivatives. Within the uncertainties of this method, we have demonstrated that this is the case (top panel of Figure 12), and that the transition energies are always around 11 keV. However, it is clear that there are substantial error bars on the values of the transition energy ϵ'_t, which are relatively independent of whether the spectral fitting approach (model-dependent) or the semi-calibrated approach (model independent) is used. In fact it is not possible to pin down the gradual/rapid boundary within about ± 5 keV throughout most of the flare, especially near the HXR peak. This is due to the difficulty of determining the folding point of the broken line. Better data with much higher count rates and lower statistical errors are required — for example, a more intense but equally simple flare — to examine whether or not such a boundary can be more clearly identified.

To understand further the relationship between the high and low energy emission components produced presumably by two distinct electron populations through the bremsstrahlung process, we investigate the electron numbers in each population. In one version of the standard model, it is postulated that electrons are accelerated at a reconnection current sheet and the acceleration process is decoupled from the electron transport and magnetic field evolution after the reconnection (Aschwanden 1998), which would imply an ideal Neupert effect not wholly supported by observations (Veronig et al. 2005). This scenario also encounters the well-known number problem (Fletcher & Hudson 2008). Given the high energy release during some large flares (Emslie et al. 2004, 2005), energy flows likely play more important roles than nonthermal electron fluxes in our exploration of the physics in the impulsive phase. It is possible that a significant fraction of the magnetic energy is converted into particle energies after the reconnection during the relaxation of magnetic field lines. The reconnection only permits the changes of magnetic field topology and may not correspond to the dominant energy dissipation and particle acceleration process, which can proceed after the reconnection (Fletcher & Hudson 2008). In the context of stochastic particle acceleration, it is usual to assume that electrons arriving at the chromosphere are accelerated out of a population in the loop (Petrosian & Liu 2004), therefore — assuming for simplicity no magnetic convergence — the number density of non-thermal electrons should be no larger than the loop number density. Sui et al. (2002) suggested that high-energy electrons might be accelerated from a cool background plasma not observed in X-rays. There is no observational evidence for

such a cold background. Theoretically, it is also difficult to understand why the acceleration should proceed in relatively cool regions given the microphysics of particle energization by electric fields is the same for both thermal and nonthermal populations. Moreover, as we will show below, the observed thermal plasma is dense enough to provide electrons responsible for the high energy emission. The assumption of a cooler background source for the high energy electrons appears to be unnecessary. In the following, we will assume that electrons producing the high energy component are accelerated from the observed thermal component. The number density of a nonthermal electron beam can be estimated as

$$n_{nth} = \frac{P_c}{\bar{E}\bar{v}_e A_{HXR}}, \tag{9}$$

where P_c is the power in electrons of energy greater than E_c, A_{HXR} is the area of HXR footpoints where electrons enter the chromosphere and can be estimated from flare images, $\bar{E}$ is the average electron energy and $\bar{v}_e$ is the corresponding electron velocity. P_c is given by

$$P_c = \frac{A_E}{\delta - 2}(E_c/\text{keV})^{-(\delta-2)}[\text{keVs}^{-1}], \tag{10}$$

where δ is the spectral index of the underlying non-thermal electron flux spectrum ($\delta = \gamma + 1$ in the collisional thick target model), A_E is a normalization parameter and is numerically related to the photon spectrum (Brown 1971; Saint-Hilaire & Benz 2005; Fletcher et al. 2007):

$$A_E = 6.44 \times 10^{33} \frac{\gamma(\gamma - 1)}{B(\gamma - 1, 1/2)} A_\epsilon, \tag{11}$$

where B is the beta function, and A_ϵ is the normalization of the power-law fit to the photon spectrum $f(\epsilon) = A_\epsilon(\epsilon/\text{keV})^{-\gamma}$ (in photons s^{-1}cm^{-2}keV^{-1}). It can be shown that $\bar{E} \equiv \int_{E_c}^{\infty} F(E)EdE / \int_{E_c} F(E)dE = (\delta - 1)E_c/(\delta - 2)$ where $F(E) = A_E(E/\text{keV})^{-\delta}$ is the electron flux injected into the footpoints (Brown 1971). $\bar{v}_e \equiv \int_{E_c}^{\infty} F(E)dE / \int_{E_c}^{\infty} F(E)/v_e(E)dE = (\delta - 1/2)v_e(E_c)/(\delta - 1)$, where we have assumed the nonthermal electron distribution is given by $F(E)/(v_e(E)A_{HXR})$.

The thermal electron number density is estimated as $n_{th} = (EM/V_{SXR})^{1/2}$, where EM is the emission measure of the thermal component and V_{SXR} is the volume of the SXR thermal coronal loop. For the sake of simplicity, V_{SXR} is evaluated as $A_{SXR}^{3/2}$ where A_{SXR} is the projected area of the observed thermal coronal source. The areas within the 30% contours of the maximum value of 25-100 keV (for HXR source) and 6-9 keV (for SXR source) images can be obtained from the Pixon images directly. From the peak-time 20-second integrated image shown in Figure 2, we estimate A_{HXR} to be 20 square arcsec, A_{SXR} to be 100 square arcsec, and V_{SXR} is then about 1000 cubic arcsec. The corresponding n_{th} is greater than $\sim 10^{11}$ cm^{-3}.

The fraction of the thermal electrons accelerated into a non-thermal distribution α should be less than 1. We then have $n_{nth} \leq n_{th}$ and

$$\left(\frac{E_c}{\text{keV}}\right)^{-\delta+1/2} = \alpha \left(\frac{2EM}{m_e}\right)^{1/2} \frac{\delta - 1/2}{A_E} \frac{A_{HXR}}{V_{SXR}^{1/2}}. \tag{12}$$

Setting $\alpha = 1$, which would correspond to the minimum possible value of E_c, and with the parameters EM, γ, A_ϵ from Section 3.3, we calculate the low limit of E_c in each 4 second time bin of the spectral fitting. A comparison of low limit of E_c and the transition energies derived from variability of the semi-calibrated data (ϵ'_{t1}), the modelled spectral data (ϵ'_{t2}) and from the isothermal plus power-law spectral fit (ϵ_t) is presented in Figure 12. At the peak of the flare, the minimum possible E_c is around 5.2 keV, and throughout the event it is always smaller than the transition energy ϵ_t, which is around 11 keV. This is fully consistent with the stochastic acceleration model where non-thermal electrons are accelerated from a thermal background (Benz 1977; Petrosian & Liu 2004; Grigis & Benz 2006). We note that δ is always greater than 4 for this flare, the E_c obtained with equation (12) is rather insensitive to the poorly-determined source size A_{HXR} and A_{SXR}.

Rearranging Equation (12), and keeping other factors constant, α and E_c vary as $\alpha \propto E_c^{-(\delta-1/2)}$. If we set the low-energy cutoff $E_c \sim \epsilon_t \sim 10$ keV, with the low limit of $E_c = 5$ keV at $\alpha = 1$ for the flare peak where $\delta = \gamma + 1 = 4.3$, this gives $\alpha = 0.07$. In other words, accelerating 7% of the hot thermal distribution in the loop would satisfy the footpoint requirements. One may further assume that these accelerated electrons come from the high energy tail of the thermal distribution. In the tail of a Maxwellian, the fraction α_χ of electrons with energy above $E = \chi kT$ is $\alpha_\chi = \sqrt{4\chi/\pi}\exp(-\chi)$, so $\alpha = 0.07$ corresponds to $\chi = 3.4$. Since $kT = 1.5$ keV, the non-thermal population would correspond to the accelerated tail of electrons with initial energy above 5.1 keV. This in turn sets a requirement that the acceleration timescale would have to be less than the electron-electron Coulomb collision timescale τ_{ee} for an electron of energy 5.1 keV in a Maxwellian plasma of temperature 1.5 keV and density $4.5 \times 10^{10}\text{cm}^{-3}$ (using EM, V_{SXR} determined above). The value of τ_{ee} for an electron in the core of such a distribution is 0.02 s, and that for an electron of energy χkT is approximately $\chi^{3/2}\tau_{ee}$ or 0.13 s in this case. Note that this threshold energy should not be compared with the transition energies in the overall photon spectra directly. The electron transport and X-ray emission processes will make the transition energy in the electron population different from that of the emitted photons. In the context of stochastic acceleration in the flare loop, a higher break energy in the overall photon spectrum than in the electron distribution in the corona acceleration site implies that the electron escape timescale from the acceleration site to the footpoints is relatively long compared to the Coulomb collision timescale at these break energies so that the HXR fluxes from the footpoints are suppressed (Petrosian & Liu 2004).

It should here be remarked that the low values obtained for E_c call into question the application of the cold collisional thick target. Emslie (2003) shows that the cold collisional thick target loss rates are overestimated for electrons of energy less than 5 kT. Though we have put bounds on E_c, it remains a fit parameter, and one can instead consider the energetics of an injected non-thermal electron distribution extending from kT, which merges into the ambient thermal distribution. For this event at its peak ($\gamma = 3.3$) the collisional thick target power requirement above $5kT$ is 7.3×10^{28}erg s^{-1}, which is already too high compared with the total radiation energy of $\sim 10^{29}$ ergs obtained from the GOES observation. Following the calculation of Emslie (2003) gives about 35 times as much as this in total injected power above kT, which further demonstrates the necessity of going beyond the classical cold thick target model.

The discussion above assumes a beam of electrons with a power-law distribution. Considering the pitch-angle scattering, the average electron velocity will be lower giving rise to a higher local non-thermal electron density and hence a larger E_c. Indeed, X-ray images reveal more complex structure near the transition energy between thermal and non-thermal components. The separation of the emission into two distinct components is rather ambiguous near the transition energy. It is possible that this separation is an artifact of a simplified model of X-ray spectrum and the energy dependence of the rate of change of the photon fluxes. Two distinct electron populations can be due to different physical processes, which dominate at different energies, with the electron behavior varying considerably from low to high energies and the apparent distinction between the low and high energy emission components being just a consequence of these processes.

5.   Conclusions

We have developed a new method to study in detail the temporal evolution of thermal and non-thermal photon fluxes in solar flares. The application of this method to a flare on Feburary 20 2002 demonstrates that as expected, the low energy part of the spectrum evolves slowly, and the high energy part evolves rapidly, with an intermediate range between a few keV and 20 keV where the behavior is in transition. The data support the scenario in which the non-thermal component of the flare spectrum is impulsive, and the thermal component is gradual, in that the transition energies between these two behaviors are the same within errors whether examined in time or in energy.

However, although in the spectral fitting exercise it is possible to make a clean separation between a non-thermal, impulsive component, and a thermal, gradual component, time evolution gives a more ambiguous picture, due to the large error bars. Imaging is also

ambiguous, with no clear distinction between footpoints and loops in the energy range around 9-25 keV. Therefore we must leave open the possibility that the electrons form a continuous distribution over this range. Further studies with larger flares should help to improve the precision with which we can identify the transition between gradual and impulsive behavior.

Finally, the presence of a single pivot point throughout the flare is not supported by our analysis, though a pivot 'range' is. There is some evidence of a slightly higher value for this pivot range in the decay phase than in the rise phase.

REFERENCES

Aschwanden, M. J. 1998, ApJ, 502, 455

—. 2002, Space Sci. Rev., 101, 1

—. 2005, Physics of the Solar Corona. An Introduction with Problems and Solutions (2nd edition)

Aschwanden, M. J., Brown, J. C., & Kontar, E. P. 2002, Sol. Phys., 210, 383

Aschwanden, M. J., Kosugi, T., Hudson, H. S., Wills, M. J., & Schwartz, R. A. 1996a, ApJ, 470, 1198

Aschwanden, M. J., Wills, M. J., Hudson, H. S., Kosugi, T., & Schwartz, R. A. 1996b, ApJ, 468, 398

Bai, T., & Ramaty, R. 1979, ApJ, 227, 1072

Battaglia, M., & Benz, A. 2006, Astronomy and astrophysics, 456, 751

Battaglia, M., Fletcher, L., & Benz, A. O. 2009, A&A, 498, 891

Benz, A. O. 1977, ApJ, 211, 270

Brown, J. 1971, Sol. Phys., 18, 489

Dennis, B. R., & Zarro, D. M. 1993, Sol. Phys., 146, 177

Dere, K. P., Landi, E., Young, P. R., Del Zanna, G., Landini, M., & Mason, H. E. 2009, A&A, 498, 915

Emslie, A. G. 2003, ApJ, 595, L119

Emslie, A. G., Dennis, B. R., Holman, G. D., & Hudson, H. S. 2005, Journal of Geophysical Research (Space Physics), 110, 11103

Emslie, A. G., Kucharek, H., Dennis, B. R., Gopalswamy, N., Holman, G. D., Share, G. H., Vourlidas, A., Forbes, T. G., Gallagher, P. T., Mason, G. M., Metcalf, T. R., Mewaldt, R. A., Murphy, R. J., Schwartz, R. A., & Zurbuchen, T. H. 2004, Journal of Geophysical Research (Space Physics), 109, 10104

Feldman, U., Dammasch, I., Landi, E., & Doschek, G. A. 2004, ApJ, 609, 439

Fisher, G. H. 1989, ApJ, 346, 1019

Fletcher, L., Hannah, I. G., Hudson, H. S., & Metcalf, T. R. 2007, ApJ, 656, 1187

Fletcher, L., & Hudson, H. S. 2008, ApJ, 675, 1645

Gallagher, P. T., Dennis, B. R., Krucker, S., Schwartz, R. A., & Tolbert, A. K. 2002, Sol. Phys., 210, 341

Gan, W. 1998, Astrophysics and Space Science, 260, 515

Grigis, P. C., & Benz, A. O. 2004, A&A, 426, 1093

—. 2005, A&A, 434, 1173

—. 2006, A&A, 458, 641

Hannah, I. G., Kontar, E. P., & Sirenko, O. K. 2009, ApJ, 707, L45

Kane, S. R., & Anderson, K. A. 1970, ApJ, 162, 1003

Kontar, E., & MacKinnon, A. 2005, Solar Physics, 227, 299

Kontar, E. P., Dickson, E., & Kašparová, J. 2008, Sol. Phys., 252, 139

Krucker, S., Battaglia, M., Cargill, P. J., Fletcher, L., Hudson, H. S., MacKinnon, A. L., Masuda, S., Sui, L., Tomczak, M., Veronig, A. L., Vlahos, L., & White, S. M. 2008, A&A Rev., 16, 155

Lin, R., Dennis, B., Hurford, G., Smith, D., Zehnder, A., Harvey, P., Curtis, D., Pankow, D., Turin, P., Bester, M., et al. 2002, Solar Physics, 210, 3

Liu, S., & Fletcher, L. 2009, ApJ, 701, L34

Liu, S., Han, F., & Fletcher, L. 2010, ApJ, 709, 58

McAteer, R. T. J., Young, C. A., Ireland, J., & Gallagher, P. T. 2007, ApJ, 662, 691

McTiernan, J. M., Fisher, G. H., & Li, P. 1999, ApJ, 514, 472

Miller, J. A., Cargill, P. J., Emslie, A. G., Holman, G. D., Dennis, B. R., LaRosa, T. N., Winglee, R. M., Benka, S. G., & Tsuneta, S. 1997, J. Geophys. Res., 102, 14631

Mrozek, T., & Tomczak, M. 2004, A&A, 415, 377

Neupert, W. M. 1968, ApJ, 153, L59+

Petrosian, V. 1973, ApJ, 186, 291

Petrosian, V., & Liu, S. 2004, ApJ, 610, 550

Pina, R. K., & Puetter, R. C. 1993, PASP, 105, 630

Saint-Hilaire, P., & Benz, A. O. 2005, A&A, 435, 743

Smith, D., Lin, R., Turin, P., Curtis, D., Primbsch, J., Campbell, R., Abiad, R., Schroeder, P., Cork, C., Hull, E., et al. 2002, Solar Physics, 210, 33

Sui, L., Holman, G. D., Dennis, B. R., Krucker, S., Schwartz, R. A., & Tolbert, K. 2002, Sol. Phys., 210, 245

Veronig, A., Vršnak, B., Dennis, B. R., Temmer, M., Hanslmeier, A., & Magdalenić, J. 2002, A&A, 392, 699

Veronig, A. M., Brown, J. C., Dennis, B. R., Schwartz, R. A., Sui, L., & Tolbert, A. K. 2005, ApJ, 621, 482